

1 High-order dynamic neural correlations reflect naturalistic 2 processing in humans

Lucy L. W. Owen¹, Thomas H. Chang^{1,2}, and Jeremy R. Manning^{1,†}

¹Department of Psychological and Brain Sciences,
Dartmouth College, Hanover, NH

³Amazon.com, Seattle, WA

[†]Address correspondence to jeremy.r.manning@dartmouth.edu

August 1, 2019

Abstract

Our thoughts arise from coordinated activity patterns across our brain. We examined high-order dynamic correlations in functional neuroimaging data collected as human participants listened to different auditory stimuli varying in cognitive richness, along with an additional resting state condition. Our approach combines a kernel-based method for estimating the dynamic functional correlations that are similar (within task) across participants, along with a dimensionality reduction approach that enables us to efficiently compute high-order correlations in the data. We trained classifiers to decode the precise time, relative to the start of the stimulus, when a given neural pattern was recorded. We trained these classifiers using the neural activity timeseries, first-order dynamic correlations, and higher-order correlations (up to tenth-order correlations), and asked which types of features led to the highest decoding accuracy. We found that higher-order correlations consistently yielded higher decoding accuracy for the most cognitively rich condition of the experiment, whereas first-order correlations or raw data yielded the highest decoding accuracy at for the less cognitively rich conditions as well as rest.

18 Introduction

To understand the neuronal computations that support cognition, we must understand the cooperative dynamics of populations of neurons. These populations of neurons interact within each brain structure, and the structures interact to form complex and dynamic networks. These interactions, at each scale, vary according to the functions our brains are carrying out and recent work has shown these dynamic complex patterns support consciousness (Demertzi et al., 2019).

In the last several decades, advances in functional magnetic resonance image (fMRI) analyses have evolved to better characterize these interactions of brain structures. As Turk-Browne (2013) outlines, analyses using multivariate patterns of activity have given an advance over univariate activity patterns because they allow relative contributions of voxels to be combined and better assess distributed representations. Resting-state connectivity (RS) fMRI, which is the temporal correlation of regions during rest, has shed light on the rich and complex spatiotemporal organization of spontaneous brain activity. Functional connectivity

30 (FC) has further characterized the cognitive state dependency of this network organization.

31 Recent work has shown that FC fluctuates over time (Chang & Glover, 2010) (Lurie et al., 2018, for
32 review), and the assumed stationarity of these analyses may be too simple to capture the dynamic nature
33 of brain activity. Additionally, recent work has shown that temporal variability in functional connectivity
34 predicts attention task performance (Fong et al., 2019) and that dynamic correlations between multivariate
35 voxel patterns can add an additional boost compared to static multivariate voxel patterns alone (Manning
36 et al., 2018).

37 Following this line of reasoning, we expect higher-order network dynamics might provide even richer
38 insights into the neural basis of cognition. We sought to test this hypothesis by developing an approach
39 to inferring high-order network dynamics from timeseries data, validating the approach using synthetic
40 data, and then applying the approach to a neuroimaging dataset comprising data collected as participants
41 listened to a story varying in cognitive richness (Simony et al., 2016).

42 Methods

43 A major challenge to studying such patterns is that typically neither the correlations nor the hierarchical
44 organizations of those correlations may be directly observed. Rather, these fundamental properties must
45 be inferred indirectly by examining the observable parts of the system—e.g., the behaviors of the individual
46 units of that system. Here we propose a series of mathematical operations that may be used to approximate
47 dynamic correlations at a range of scales (i.e., orders of interaction).

48 There are two basic steps to our approach (Fig. 2). In the first step, we take a number-of-timepoints (T)
49 by number-of-features (F) *matrix of observations* (\mathbf{X}) and we return a T by $\frac{F^2-F}{2}$ *matrix of dynamic correlations*
50 (\mathbf{Y}_0). Here \mathbf{Y}_0 describes, at each moment, how all of the features (columns of \mathbf{X}) are inferred to be interacting.
51 (Since the interactions are assumed to be non-recurrent and symmetric, only the upper triangle of the full
52 correlation matrix is computed.) In the second step, we project \mathbf{Y}_0 onto an F -dimensional space, resulting in
53 a new T by F matrix \mathbf{Y}_1 . Note that \mathbf{Y}_1 contains information about the correlation dynamics present in \mathbf{X} , but
54 represented in a compressed number of dimensions. By repeatedly applying these two steps in sequence,
55 we can examine and explore higher order dynamic correlations in \mathbf{X} .

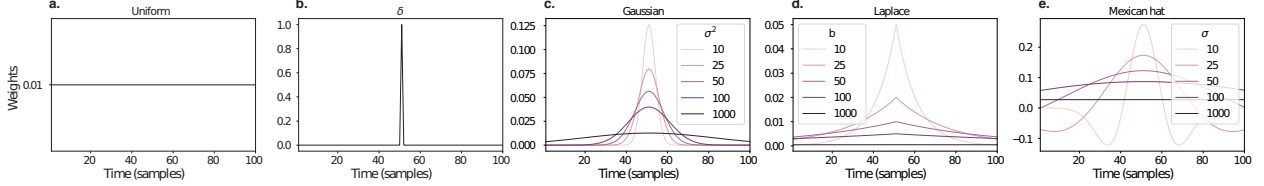


Figure 1: **Examples of time-varying weights.** Each panel displays per-timepoint weights at $t = 50$, evaluated for 100 timepoints (1, ..., 100). **a. Uniform weights.** The weights are timepoint-invariant; observations at all timepoints are weighted equally, and do not change as a function of t . This is a special case of weight function that reduces dynamic correlations to static correlations. **b. Dirac delta function.** Only the observation at timepoint t is given weight (of 1), and weights for observations at all other timepoints are set to 0. **c. Gaussian weights.** Each observation's weights fall off in time according to a Gaussian probability density function centered on $\mu = t$. Weights derived using several different example variance parameters (σ^2) are displayed. **d. Laplace weights.** Each observation's weights fall off in time according to a Laplace probability density function centered on $\mu = t$. Weights derived using several different example scale parameters (b) are displayed. **e. Mexican hat (Ricker wavelet) weights.** Each observation's weights fall off in time according to a Ricker wavelet centered on t . This function highlights the *contrasts* between local versus surrounding activity patterns in estimating dynamic correlations. Weights derived using several different example width parameters (σ) are displayed.

56 Dynamic correlations

Given a matrix of observations, we can compute the (static) correlations between any pair of observations, \mathbf{X}_i and \mathbf{X}_j using:

$$\text{corr}(\mathbf{X}_i, \mathbf{X}_j) = \frac{\sum_{t=1}^T (\mathbf{X}_i(t) - \bar{\mathbf{X}}_i)(\mathbf{X}_j(t) - \bar{\mathbf{X}}_j)}{\sqrt{\sum_{t=1}^T \sigma_{\mathbf{X}_i}^2 \sigma_{\mathbf{X}_j}^2}}, \text{ where} \quad (1)$$

$$\bar{\mathbf{X}}_k = \sum_{t=1}^T \mathbf{X}_k(t), \text{ and} \quad (2)$$

$$\sigma_{\mathbf{X}_k}^2 = \sum_{t=1}^T (\mathbf{X}_k(t) - \bar{\mathbf{X}}_k)^2 \quad (3)$$

57 We can generalize this formula to compute time-varying correlations by incorporating a *weight function*
 58 that takes a time t as input, and returns how much the observed data every timepoint (including t) contribute
 59 to the correlations at time t (Fig. 1).

Given a weight function $w(t)$ for timepoint t , evaluated at timepoints in the interval $[1, \dots, T]$, we can

extend the static correlation formula in Equation 2 to reflect an *instantaneous correlation* at timepoint t :

$$\text{timecorr}(\mathbf{X}_i, \mathbf{X}_j, t) = \frac{\sum_{t=1}^T (\mathbf{X}_i(t) - \tilde{\mathbf{X}}_i(t))(\mathbf{X}_j(t) - \tilde{\mathbf{X}}_j(t))}{\sqrt{\sum_{t=1}^T \tilde{\sigma}_{\mathbf{X}_i}^2(t) \tilde{\sigma}_{\mathbf{X}_j}^2(t)}}, \text{ where} \quad (4)$$

$$\tilde{\mathbf{X}}_k(t) = \sum_{i=1}^T w(t, i) \mathbf{X}_k(i), \quad (5)$$

$$\tilde{\sigma}_{\mathbf{X}_k}^2(t) = \sum_{i=1}^T (\mathbf{X}_k(i) - \tilde{\mathbf{X}}_k(t))^2, \quad (6)$$

- and $w(t, i)$ is shorthand for $w(t)$ evaluated at timepoint i . Equation 5 may be used to estimate the instantaneous correlations between every pair of observations, at each timepoint (i.e., \mathbf{Y}).

62 Inter-subject dynamic correlations

Equation 5 provides a means of taking a single observation matrix, \mathbf{X} and estimating the dynamic correlations from moment to moment, \mathbf{Y} . Suppose that one has access to a set of multiple observation matrices that reflect the same phenomenon. For example, one might collect neuroimaging data from several experimental participants, as each participant performs the same task (or sequence of tasks). Let $\mathbf{X}_1, \mathbf{X}_2, \dots, \mathbf{X}_P$ reflect the T by F observation matrices for each of P participants in an experiment. We can use *inter-subject functional connectivity* (ISFC; Simony et al., 2016) to compute the degree of stimulus-driven correlations reflected in the multi-participant dataset at a given timepoint t using:

$$\bar{\mathbf{C}}(t) = M \left(R \left(\frac{1}{2P} \sum_{i=1}^P Z(Y_i(t))^T + Z(Y_i(t)) \right) \right), \quad (7)$$

where M extracts and vectorizes the diagonal and upper triangle of a symmetric matrix, Z is the Fisher z-transformation (Zar, 2010):

$$Z(r) = \frac{\log(1+r) - \log(1-r)}{2} \quad (8)$$

R is the inverse of Z :

$$R(z) = \frac{\exp(2z-1)}{\exp(2z+1)}, \quad (9)$$

and $\mathbf{Y}_i(t)$ denotes the correlation matrix (Eqn. 2) between each column of \mathbf{X}_i and each column of the average observations from all *other* participants, $\bar{\mathbf{X}}_{\setminus i}$:

$$\bar{\mathbf{X}}_{\setminus i} = R \left(\frac{1}{P-1} \sum_{i \in \setminus i} Z(\mathbf{X}_i) \right), \quad (10)$$

where $\setminus i$ denotes the set of all participants other than participant i . In this way, the T by $\left(\frac{F^2-F}{2} + F\right)$ matrix $\bar{\mathbf{C}}$ is the time-varying extension of the ISFC approach developed by Simony et al. (2016).

65 Higher-order correlations

Given a timeseries of dynamic correlations (e.g., obtained using Eqn. 5), higher-order correlations reflect the dynamic correlations between columns of \mathbf{Y} . Given unlimited computing resources, one could use repeated applications of Equation 5 to estimate these higher-order correlations (i.e., substituting in the previous output, \mathbf{Y} , for the input, \mathbf{X} in the equation). However, because each output \mathbf{Y} has $O(F^2)$ columns relative to F columns in the input \mathbf{X} , the output of Equation 5 grows with the square of the number of repeated applications (total cost of computing n^{th} order correlations is $O(F^{2n})$ for $n \in \mathcal{J}, n > 0$). When F or n is large, this approach quickly becomes intractable.

To make progress in computing \mathbf{Y}_{n+1} , we can approximate \mathbf{Y}_n by computing an $O(F)$ -dimensional embedding of \mathbf{Y}_n , termed $\hat{\mathbf{Y}}_n$, and then we can apply Equation 5 to $\hat{\mathbf{Y}}_n$ rather than directly to \mathbf{Y}_n . This enables us to maintain $O(n)$ scaling with respect to n , rather than exponential scaling via the direct approach.

There are many possible methods for computing $\hat{\mathbf{Y}}_n$ from \mathbf{Y}_n , including traditional dimensionality reduction approaches and graph theory based approaches as described next. In the *Discussion* section we elaborate on other potential approaches.

79 Dimensionality reduction-based approaches to computing $\hat{\mathbf{Y}}_n$

Commonly used dimensionality reduction algorithms include Principal Components Analysis (PCA; Pearson, 1901), Probabilistic PCA (PPCA; Tipping & Bishop, 1999), Exploratory Factor Analysis (EFA; Spearman, 1904), Independent Components Analysis (ICA; Jutten & Herault, 1991; Comon et al., 1991), t -Stochastic Neighbor Embedding (t -SNE; van der Maaten & Hinton, 2008), Uniform Manifold Approximation and Projection (UMAP; McInnes & Healy, 2018), non-negative matrix factorization (NMF; Lee & Seung, 1999), Topographic Factor Analysis (TFA) Manning et al. (2014), Hierarchical Topographic Factor analysis (HTFA) Manning et al. (2018), Topographic Latent Source Analysis (TLSA) Gershman et al. (2011), Dictionary learning (J. B. Mairal et al., 2009; J. Mairal et al., 2009), deep autoencoders (Hinton & Salakhutdinov,

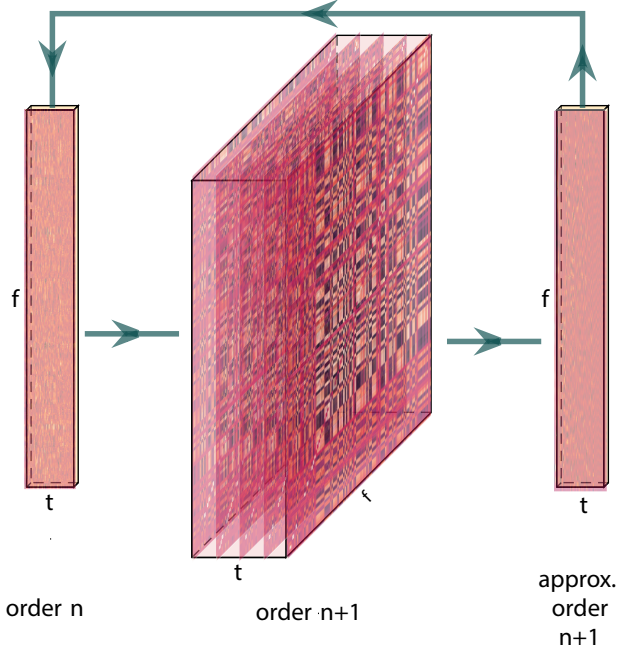


Figure 2: Computing higher order correlations. Dynamic correlations are computed then approximated to the same size as original data using dimensionality reduction. This process is repeated, and can be used to compute up to any arbitrary order with computations scaling linearly (as opposed to exponentially) with order.

88 2006), among others. While complete characterizations of each of these algorithms is beyond the scope of
 89 the present manuscript, the general intuition driving these approaches is to compute the $\hat{\mathbf{Y}}$ with i columns
 90 that is closest to the original \mathbf{Y} with j columns, and where (typically) $i \ll j$. The different approaches place
 91 different constraints on what properties $\hat{\mathbf{Y}}$ must satisfy and which aspects of the data are compared (and
 92 how) to characterize the match between $\hat{\mathbf{Y}}$ and \mathbf{Y} .

93 Applying dimensionality reduction algorithms to \mathbf{Y} yields a $\hat{\mathbf{Y}}$ whose columns reflect weighted combi-
 94 nations (or nonlinear transformations) of the original columns of \mathbf{Y} . This has two main consequences. First,
 95 with each repeated dimensionality reduction, the resulting $\hat{\mathbf{Y}}_n$ has lower and lower fidelity (with respect to
 96 what the “true” \mathbf{Y}_n might have looked like without using dimensionality reduction to maintain scalability).
 97 In other words, computing $\hat{\mathbf{Y}}_n$ is a lossy operation. Second, whereas the columns of \mathbf{Y}_n may be mapped
 98 directly onto pairs of columns of \mathbf{Y}_{n-1} , that mapping either becomes less cleanly defined in $\hat{\mathbf{Y}}_n$ due to the
 99 reweightings and/or nonlinear transformations.

100 **Graph theory-based approaches to computing $\hat{\mathbf{Y}}_n$**

101 Graph theoretic measures take as input a matrix of interactions (e.g., using the above notation, an $F \times F$
 102 correlation matrix or binarized correlation matrix reconstituted from a single timepoint’s row of \mathbf{Y}) and

103 return as output a set of F measures describing how each node (feature) sits within that interactions matrix
104 with respect to the rest of the population. Common measures include betweenness centrality (the proportion
105 of shortest paths between each pair of nodes in the population that involves the given node in question; e.g.,
106 Newman, 2005; Opsahl et al., 2010; Barthélemy, 2004; Geisberger et al., 2008; Freeman, 1977); diversity and
107 dissimilarity (characterizations of how differently connected a given node is from others in the population;
108 e.g., Rao, 1982; Lin, 2009; Ricotta & Szeidl, 2006); Eigenvector centrality and pagerank centrality (measures of
109 how influential a given node is within the broader network; e.g., Newman, 2008; Bonacich, 2007; Lohmann
110 et al., 2010; Halu et al., 2013); transfer entropy and flow coefficients (a measure of how much information is
111 flowing from a given node to other nodes in the network; e.g., Honey et al., 2007; Schreiber, 2000); k -coreness
112 centrality (a measure of the connectivity of a node within its local sub-graph; e.g., Alvarez-Hamelin et al.,
113 2005; Christakis & Fowler, 2010); within-module degree (a measure of how many connections a node has to
114 its close neighbors in the network; e.g., Rubinov & Sporns, 2010); participation coefficient (a measure of the
115 diversity of a node's connections to different sub-graphs in the network; e.g., Rubinov & Sporns, 2010); and
116 sub-graph centrality (a measure of a node's participation in all of the network's sub-graphs; e.g., Estrada &
117 Rodríguez-Velázquez, 2005).

118 As an alternative to the above dimensionality reduction approach to embedding \mathbf{Y}_n in a lower-dimensional
119 space, but still allowing for scalable explorations of higher-order structure in the data, we also explore using
120 the above graph theoretic measures as a means of obtaining $\hat{\mathbf{Y}}_n$. In particular: for a given graph theoretic
121 measure, $\eta : \mathcal{R}^{F \times F} \rightarrow \mathcal{R}^F$, we can use η to transform each row of \mathbf{Y}_n in a way that characterizes the cor-
122 responding graph-theoretic properties of each column. Whereas the dimensionality reduction approach
123 to computing $\hat{\mathbf{Y}}_n$ is lossy, the graph-theory approach is lossless. However, whereas the dimensionality
124 reduction approach maintains ties (direct or indirect) to the original activity patterns reflected in \mathbf{Y}_{n-1} , the
125 graph-theory approach does not. Instead, the graph-theory characterizes the nature and timecourse of each
126 feature's *participation* in the network.

127 Evaluation metrics

128 We evaluate our approach to extracting dynamic correlations and higher-order correlations using several
129 metrics detailed next. First, we generated synthetic data using known time-varying correlations, and then
130 we evaluated the fidelity with which Equation 5 could recover those correlations (for synthetic datasets
131 with different properties, and using different kernels to define the weights; Fig. 1). We then turned to a
132 series of analyses on a (real) neuroimaging dataset where the ground truth correlations were *not* known.
133 We evaluated whether the recovered correlations could be used to accurately label held-out neuroimaging

134 data with the time at which it was collected. We used this latter evaluations (using timepoint decoding)
135 as a proxy for gauging how much explanatory power the recovered correlations held with respect to the
136 observed data.

137 **Generating synthetic data**

138 To explore recovery of a constant covariance (Fig. 3, a.), we generated synthetic data sampled from a constant
139 covariance matrix. To do this, we created one random covariance matrix, K , with 50 features, and for each
140 of the 300 timepoints we sampled from a Gaussian distribution centered on K . Similarly, we generated
141 synthetic data sampled from a random covariance matrix (Fig. 3, b.) by creating a new random covariance
142 matrix $K(t)$, for each of the 300 timepoints and sampled from a Gaussian distribution centered on $K(t)$.

To generate synthetic data from a dynamically changing covariance matrix (Fig. 3, c.), we generated two
random covariance matrices, K_1 and K_2 . We then computed a weighted average covariance matrix for each
of the 300 timepoint, $K(t)$, by taking the linearly spaced weights (w) of the two random matrices,

$$K(t) = w(t) * K_1 + (1 - w(t)) * K_2, \quad (11)$$

$$(12)$$

143 and for each of the 300 timepoints sampled from a Gaussian distribution centered on $K(t)$.

144 Lastly, for the synthetic data containing block structure (Fig. 3, d.), we followed the same process of
145 creating synthetic data sampled from a constant covariance matrix (see above) but sampled from a new
146 random covariance matrix after 60 consecutive timepoints. We then pieced the blocks together to create a
147 synthetic dataset with 300 total timepoints but drawn from 5 separate covariance matrices.

148 **Recovery of ground truth parameters from synthetic data**

149 We applied timecorr, using delta and gaussian (width = 10) kernels Fig. 1 to each of these synthetic datasets,
150 then correlated each recovered correlation matrix with the ground truth. We repeated this process 10 times
151 and explored how recovery varies with the kernel and the specific structure of the data. For the ramping
152 synthetic dataset (Fig. 3, c.) and for the block synthetic dataset (Fig. 3, d.) we made further comparisons
153 of the timecorr recovered correlation matrices. We compared the ramping recovered correlation matrices to
154 only the first random covariance matrix K_1 (First, Fig. 3, c.) and to only the last random covariance matrix
155 K_2 (Last, Fig. 3, c.) from Equation 12. We also compared the block recovered correlation matrices in to the
156 block specific covariance matrix (Block 1-5, Fig. 3, d.).

157 **Timepoint decoding**

158 To explore how higher-order structure varies with stimulus structure and complexity, we used a previous
159 neuroimaging dataset Simony et al. (2016) in which participants listened to an audio recording of a story;
160 36 participants listen to an intact version of the story, 17 participants listen to time-scrambled recordings of
161 the same story where paragraphs were scrambled, 36 participants listen to word-scrambled version and 36
162 participants lay in rest condition.

163 Prior work has shown participants share similar neural responses to richly structured stimuli when
164 compared to stimuli with less structure. To assess whether the moment-by-moment higher order correlations
165 were reliably preserved across participants, we used inter-subject functional connectivity (ISFC) to isolate
166 the time-varying correlational structure (functional connectivity patterns that were specifically driven by
167 the story participants listened to. Following the analyses conducted by (HTFA) Manning et al. (2018), we
168 first applied *hierarchical topographic factor analysis* (HTFA) to the fMRI datasets to obtain a time series of
169 700 node activities for every participant. We then computed the dynamic weighted ISFC using a range of
170 kernels and widths. Specifically, we used Gaussian, Laplace, and mexican hat kernels, as well as widths of
171 5, 10, 20, and 50. We then approximated these dynamic correlation using two reduction measures, PCA and
172 eigenvector centrality, and computed the dynamic weighted ISFC on the approximations. We repeated this
173 process up to 10th order approximated correlations.

174 To assess decoding accuracy, we randomly divided participants for each stimulus into training and
175 testing groups. For the zeroth order, we computed the mean factor activity for each group. For all subsequent
176 orders up to the tenth order, we computed the mean approximated dynamic ISFC of factor activity for each
177 group. To assess how additional higher-order correlations contribute to decoding accuracy, for each order
178 we included a weighted-mixture (described below) of the activity patterns of all previous orders. For each
179 group of participants in turn, we compared these activity patterns (using Pearson correlations) to estimate
180 the story times each pattern corresponded to. Specifically, we asked, for each timepoint: what are the
181 correlations between the first group's and second group's activity patterns at each order. We note that the
182 decoding test we used is a conservative in which we count a timepoint label as incorrect if it is not an exact
183 match.

184 For each order we obtained the weighted-mixture of the correlation matrices for the current order and
185 all previous orders using mixing parameter, ϕ , where $0 < \phi < 1$ reflects a weighted mixture of order based
186 decoding Fig. 4 Panel c.). We calculated ϕ , by subdividing the training group and using the quasi-Newton
187 method of Broyden, Fletcher, Goldfarb, and Shanno (BFGS (Nocedal & Wright, 2006)) for optimization. We
188 repeated this cross-validation process 10 times for each parameter set.

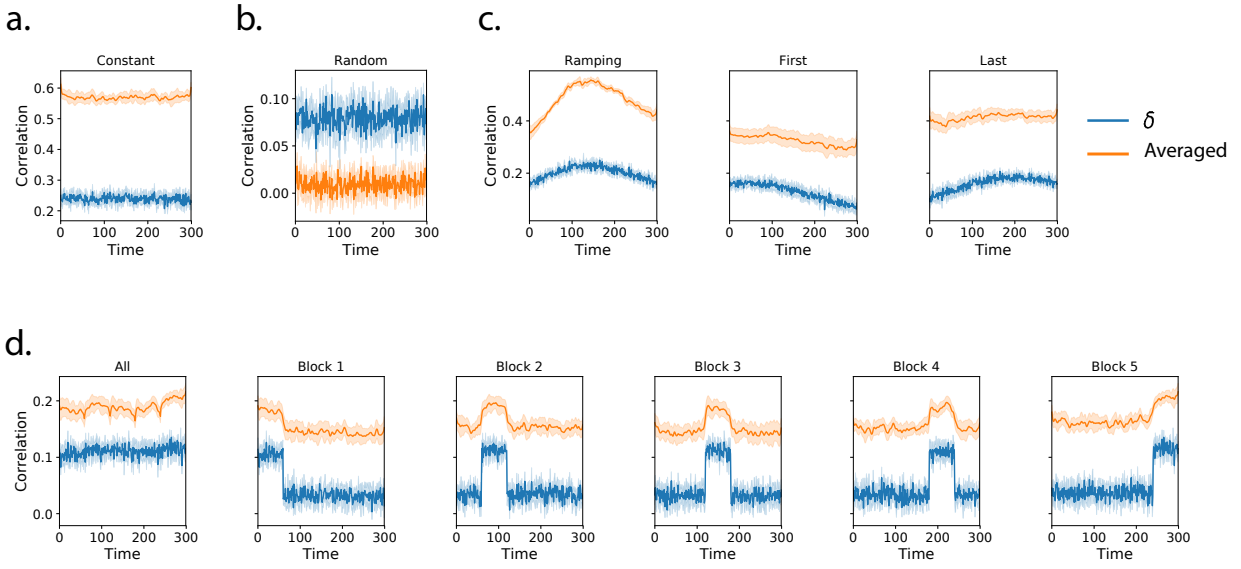


Figure 3: **Dynamic correlation recovery with synthetic data.** Using synthetic data containing different underlying correlational structure, we test how well we can recover dynamic correlation matrices using different kernels when compared to ground truth. We compare the results using a delta kernel with averaged results from several kernels (Gaussian, Laplace, and mexican hat) and several widths (5, 10, 20, and 50). We plot recovery of datasets containing the following underlying structure: **a. Constant.** **b. Random.** **c. Ramping.** **d. Block.**

189 Results

190 Synthetic data

191 To assess the performance of dynamic correlation recovery using `timecorr`, we varied width the kernel and
 192 the specific structure of the data. We applied `timecorr`, using delta and gaussian kernels Fig. 1) to each of
 193 the following synthetic datasets: constant, random, ramping, and block. We then correlated each recovered
 194 correlation matrix with the ground truth.

195 For the constant synthetic dataset, a gaussian kernel (width=10) outperformed the delta kernel (Fig. 3,
 196 a.). This is in contrast with the random synthetic dataset, for which the delta kernel best captures the rapidly
 197 changing structure (Fig. 3, b.). For the ramping synthetic dataset, the slow changing strucutre within the
 198 data is best captured by the gaussian kernel and the best recovery occurs in the middle (Ramping, Fig. 3,
 199 c.). In addition to comparing the `timecorr` recovered correlation matrices to the ground truth, we further
 200 compared the ramping recovered correlation matrices to only the first random covariance matrix K_1 (First,
 201 Fig. 3, c.) and to only the last random covariance matrix K_2 (Last, Fig. 3, c.), both of which perform best at
 202 the beginning and end respectively.

203 Similary for the block sythetic dataset, we compared the `timecorr` recovered correlation matrices to

204 the ground truth as well as to each block-specific covariance matrix (Block 1-5, Fig. 3, d.). Although the
205 structure is changing by block, the gaussian kernel once again outperforms the delta kernel. Performance
206 does however drop near even boundaries for when using the gaussian kernel.

207 **Neuroimaging dataset (Simony et al., 2016)**

208 For our decoding analysis, we used HTFA-derived node activities Manning et al. (2018) from fMRI data
209 collected as participants listened to an audio recording of a story (intact condition; 36 participants), lis-
210 tened to time scrambled recordings of the same story (17 participants in the paragraph-scrambled condition
211 listened to the paragraphs in a randomized order and 36 in the word-scrambled condition listened to
212 the words in a randomized order), or lay resting with their eyes open in the scanner (rest condition; 36
213 participants). We sought to demonstrate how higher-order correlations may be used to examine dynamic
214 interactions of brain patterns in (real) multi-subject fMRI datasets. This story listening dataset was col-
215 lected as part of a separate study, where the full imaging parameters, image preprocessing methods, and
216 experimental details may be found (Simony et al., 2016). The dataset is available at [http://arks.prince-
217 ton.edu/ark:/88435/dsp015d86p269k](http://arks.princeton.edu/ark:/88435/dsp015d86p269k).

218 We next evaluated if our model of high-order correlations in brain activity can capture cognitively
219 relevant brain patterns. We performed a decoding analysis, using cross validation to estimate (using other
220 participants' data) which parts of the story each weighted-mixture of higher-order brain activity pattern
221 corresponded to (see *Materials and methods*). We note that our primary goal was not to achieve perfect
222 decoding accuracy, but rather to use decoding accuracy as a benchmark for assessing whether different
223 neural features specifically capture cognitively relevant brain patterns.

224 Separately for each experimental condition, we divided participants into two groups. For the zeroth
225 order, we computed the mean factor activity for each group. For all subsequent orders up to the tenth
226 order, we computed the mean approximated dynamic ISFC of factor activity for each group (see *Materials*
227 and *methods*), and combined in a weighted mixutre with all previous orders (i.e. cross-validation for the
228 second order contained a weighted-mixture of zeroth, first, and second order (Fig. 4, c.&f.). For each
229 order, we correlated the group 1 activity patterns with group 2 activity patterns. We then subdivided
230 the group 1 to obtain an optimal weighting parameter for each order's correlation matrix using the same
231 cross validation method. We used the optimal weighting parameters to obtain a weighted-mixture (see
232 *Materials and methods*) of each order's correlation matrix. Using these correlations, we labeled the group 1
233 timepoints using the group 2 timepoints with which they were most highly correlated; we then computed
234 the proportion of correctly labeled group 1 timepoints. (We also performed the symmetric analysis whereby

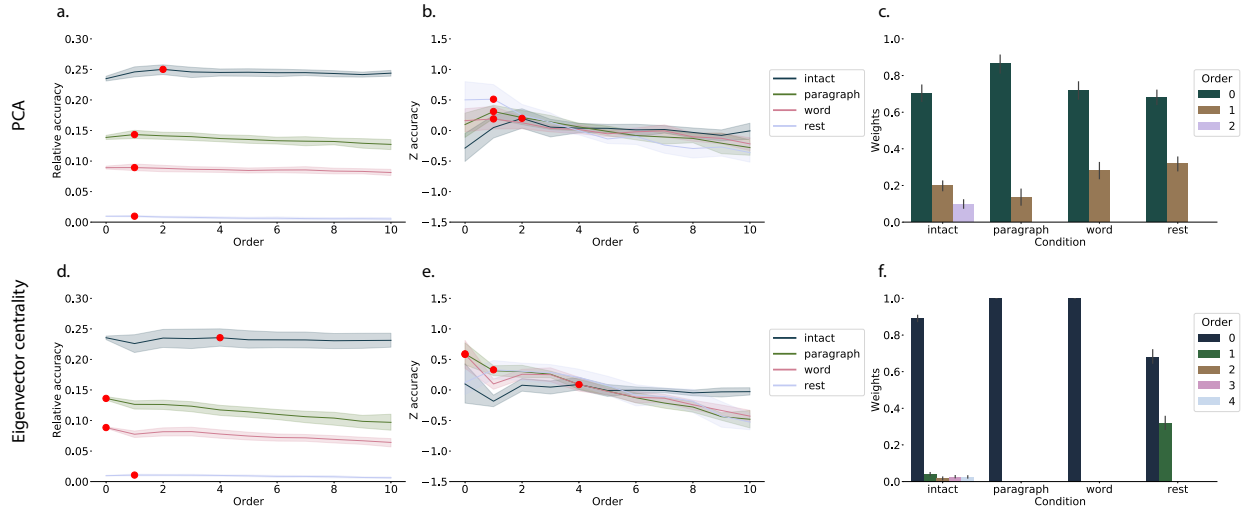


Figure 4: **Decoding by order.** **a.&d. Relative decoding accuracy by order.** Ribbons of each color display cross-validated decoding performance averaged over all parameters for each condition (intact, paragraph, word, and rest) using PCA (a.) or eigenvector centrality (d.) to approximate correlations. Decoders were trained using increasingly more higher-order information and this ribbons are displayed relative to chance at 0. The red dots indicates maximum decoding accuracy for each condition. **b.&e. Z-transformed decoding accuracy by order.** We Z-transformed the decoding accuracy by order to better visualize the order with the maximum decoding accuracy for each condition using PCA (b.) or eigenvector centrality (e.) to approximate correlations. **c.&f. Optimized weights.** Bar heights indicate the optimized mixing parameter ϕ of each contributing order up to and including the order with the maximum decoding accuracy for each contributing order using PCA (c.) or eigenvector centrality (f.) to approximate correlations. For the order with maximum decoding accuracy by condition, we show barplots of the optimized weights ϕ for each contributing order.

235 we labeled the group 2 timepoints using the group 1 timepoints as a template.) We repeated this procedure
236 100 times (randomly re-assigning participants to the two groups each time) to obtain a distribution of
237 decoding accuracies for each experimental condition. There were 272 timepoints for paragraph condition,
238 300 timepoints for intact and word conditions, and 400 timepoints for rest condition, so chance performance
239 on this decoding test is was $\frac{1}{272}$, $\frac{1}{300}$, and $\frac{1}{400}$ respectively.

240 We repeated this process for each set of parameters, varying kernel type and width, and averaged over the
241 reduction technique used to approximate the higher-order correlations (PCA Fig. 4, a.-c. and eigenvector
242 centrality Fig. 4, d.-f.). Since there is no ground truth in these analyses, and we did not know which
243 parameters best capture the data, we instead report a robustness search by averaging over the parameters
244 and reporting which results consistently showed up across all parameters.

245 The two methods used to approximate the higher-order correlations (PCA Fig. 4, a.-c. and eigenvector
246 centrality Fig. 4, d.-f.) capture different facets of the activity patterns. Using PCA, the higher-order
247 correlations are all linked to the original activity patterns, whereas eigenvector centrality breaks the
248 immediate link with specific brain areas and instead characterizes the position of the nodes in the network
249 that are similar over time.

250 We found for both PCA and eigenvector centrality, during the intact condition in the experiment,
251 classifiers that incorporated higher-order correlations yielded consistently higher accuracy than classifiers
252 trained only on lower-order patterns (Fig. 4, a.&d.). We plot the average correlations for up to the fourth
253 order for the intact condition (Fig. 5) representing the degree of agreement by location pair over time. By
254 contrast, we found that incorporating higher-order (greater than first order) correlations did not further
255 improve decoding accuracy for the other listening conditions or rest condition. This suggests that the
256 cognitive processing that supported the most cognitively rich condition involved higher-order network
257 dynamics.

258 Discussion

259 Based on prior work (Demertzis et al., 2019) and following the direction of the field (Turk-Browne, 2013)
260 we think our thoughts might be encoded in dynamic network patterns, and possibly higher order network
261 patterns (Fig. 6). We sought to test this hypothesis by developing an approach to inferring high-order
262 network dynamics from timeseries data.

263 One challenge in studying dynamic interactions is the computational resources required to calculate
264 higher-order correlations. We developed a computationally tractable model of network dynamics (Fig. 2)
265 that takes in a feature timeseries and outputs approximated first-order dynamics (i.e., dynamic functional

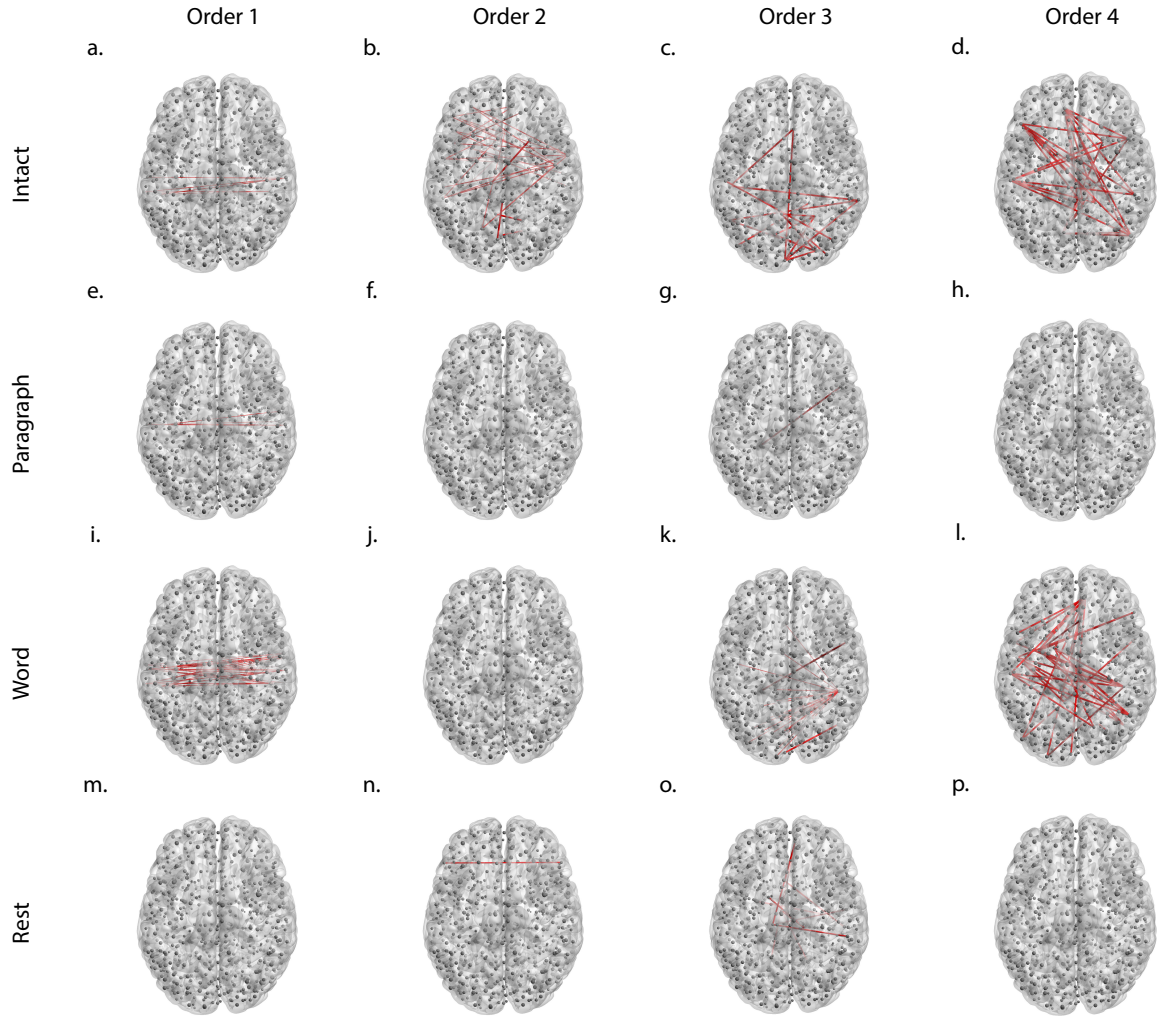


Figure 5: Average correlations by order for the intact listening condition. Using eigenvector centrality to approximate higher-order correlations for **a.-d.** intact, **e.-h.** paragraph scrambled, **i.-l.** word scrambled, and **m.-p.** rest conditions, we plot the strongest 25% absolute value mean correlation for first through fourth orders, representing the degree of agreement by location pair over time.

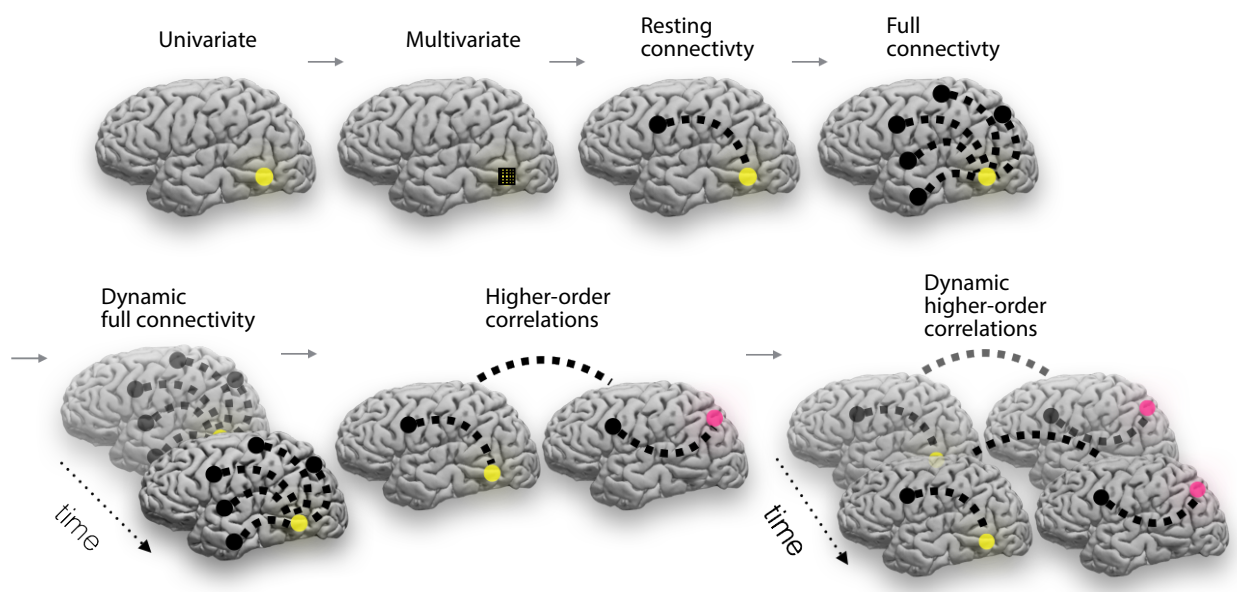


Figure 6: Direction of the field (adapted from (Turk-Browne, 2013)). The evolution of fMRI analyses started with univariate activation, which refers to the average amplitude of BOLD activity evoked by events of an experimental condition. Next, multivariate classifiers are trained on patterns of activation across voxels to decode distributed representations for specific events. The next, resting connectivity, is the temporal correlation of one or more seed regions with the remainder of the brain during rest. Additionally, task-based connectivity examines how these correlations differ by cognitive state. Following this increasing trajectory of increasing complexity, full connectivity considers all pairwise correlations in the brain, most commonly at rest. Next, dynamic full connectivity considers how full connectivity changes over time. Continuing this line of reasoning, we expect higher-order network dynamics might provide even richer insights into the neural basis of cognition.

266 correlations), second-order dynamics (reflecting homologous networks that dynamically form and disperse),
267 and higher-order network dynamics (up to tenth-order dynamic correlations).

268 We first validated our model using synthetic data, and explored how recovery varied with different
269 underlying data structures and kernels. We then applied the approach to an fMRI dataset (Simony et al.,
270 2016) in which participants listened to an audio recording of a story, as well as scrambled versions of the
271 same story (where the scrambling was applied at different temporal scales). We trained classifiers to take
272 the output of the model and decode the timepoint in the story (or scrambled story) that the participants
273 were listening to. We found that, during the intact listening condition in the experiment, classifiers that
274 incorporated higher-order correlations yielded consistently higher accuracy than classifiers trained only
275 on lower-order patterns (Fig. 4, a.&d.). By contrast, these higher-order correlations were not necessary
276 to support decoding the other listening conditions and (minimally above chance) during a control rest
277 condition. This suggests that the cognitive processing that supported the most cognitively rich listening
278 conditions involved second-order (or higher) network dynamics.

279 Although we found decoding accuracy was best when incorporating higher-order network dynamics
280 for all but rest condition, it is unclear if this is a product of the brain or the data collection technique. It could
281 be that the brain is second-order or it could be that fMRI can only reliably give second-order interactions.
282 Exploring this method with other data collection technique will be important to disentangle this question.

283 **Concluding remarks**

284 How can we better understand how brain patterns change over time? How can we quantify the potential
285 network dynamics that might be driving these changes? One way to judge the techniques of the future is
286 to look at the trajectory of the fMRI field so far has taken so far (Fig. 2). The field started with univariate
287 activation, measuring the average activity for each voxel. Analyses of multivariate activation followed,
288 looking at spatial patterns of activity over voxels. Next, correlations of activity were explored, first with
289 measures like resting connectivity that take temporal correlation between a seed voxel and all other voxels
290 then with full connectivity that measure all pairwise correlations. Additionally, this path of increasing
291 complexity also moved from static to dynamic measurements. One logical next step in this trajectory would
292 be dynamic higher-order correlations. We have created a method to support these calculations by scalably
293 approximating dynamic higher-order correlations.

294 **Acknowledgements**

295 We acknowledge discussions with Luke Chang, Hany Farid, Paxton Fitzpatrick, Andrew Heusser, Eshin
296 Jolly, Qiang Liu, Matthijs van der Meer, Judith Mildner, Gina Notaro, Stephen Satterthwaite, Emily Whitaker,
297 Weizhen Xie, and Kirsten Ziman. Our work was supported in part by NSF EPSCoR Award Number 1632738
298 to J.R.M. and by a sub-award of DARPA RAM Cooperative Agreement N66001-14-2-4-032 to J.R.M. The
299 content is solely the responsibility of the authors and does not necessarily represent the official views of our
300 supporting organizations.

301 **Author contributions**

302 Concept: J.R.M. Implementation: T.H.C., L.L.W.O., and J.R.M. Analyses: L.L.W.O and J.R.M.

303 **References**

- 304 Alvarez-Hamelin, I., Dall'Asta, L., Barrat, A., & Vespignani, A. (2005). *k*-corr decomposition: a tool for the
305 visualization of large scale networks. *arXiv*, cs/0504107v2.
- 306 Barthélémy, M. (2004). Betweenness centrality in large complex networks. *European Physical Journal B*, 38,
307 163–168.
- 308 Bonacich, P. (2007). Some unique properties of eigenvector centrality. *Social Networks*, 29(4), 555–564.
- 309 Chang, C., & Glover, G. H. (2010). Time-frequency dynamics of resting-state brain connectivity measured
310 with fMRI. *NeuroImage*, 50, 81–98.
- 311 Christakis, N. A., & Fowler, J. H. (2010). Social network sensors for early detection of contagious outbreaks.
312 *PLoS One*, 5(9), e12948.
- 313 Comon, P., Jutten, C., & Herault, J. (1991). Blind separation of sources, part II: Problems statement. *Signal
314 Processing*, 24(1), 11 - 20.
- 315 Demertzi, A., Tagliazucchi, E., Dehaene, S., Deco, G., Barttfeld, P., Raimondo, F., . . . Sitt, J. D. (2019). Human
316 consciousness is supported by dynamic complex patterns of brain signal coordination. *Science Advances*,
317 5(2), eaat7603.
- 318 Estrada, E., & Rodríguez-Velázquez, J. A. (2005). Subgraph centrality in complex networks. *Physical Review
319 E*, 71(5), 056103.

- 320 Fong, A. H. C., Yoo, K., Rosenberg, M. D., Zhang, S., Li, C.-S. R., Scheinost, D., ... Chun, M. M. (2019).
321 Dynamic functional connectivity during task performance and rest predicts individual differences in
322 attention across studies. *NeuroImage*, 188, 14–25.
- 323 Freeman, L. C. (1977). A set of measures of centrality based on betweenness. *Sociometry*, 40(1), 35–41.
- 324 Geisberger, R., Sanders, P., & Schultes, D. (2008). Better approximation of betweenness centrality. *Proceedings*
325 *of the meeting on Algorithm Engineering and Experiments*, 90–100.
- 326 Gershman, S., Blei, D., Pereira, F., & Norman, K. (2011). A topographic latent source model for fMRI data.
327 *NeuroImage*, 57, 89–100.
- 328 Halu, A., Mondragón, R. J., Panzarasa, P., & Bianconi, G. (2013). Multiplex PageRank. *PLoS One*, 8(10),
329 e78293.
- 330 Hinton, G. E., & Salakhutdinov, R. R. (2006). Reducing the dimensionality of data with neural networks.
331 *Science*, 313(5786), 504–507.
- 332 Honey, C. J., Kotter, R., Breakspear, M., & Sporns, O. (2007). Network structure of cerebral cortex shapes
333 functional connectivity on multiple time scales. *Proceedings of the National Academy of Science USA*, 104(24),
334 10240–10245.
- 335 Jutten, C., & Herault, J. (1991). Blind separation of sources, part I: An adaptive algorithm based on
336 neuromimetic architecture. *Signal Processing*, 24(1), 1–10.
- 337 Lee, D. D., & Seung, H. S. (1999). Learning the parts of objects by non-negative matrix factorization. *Nature*,
338 401, 788–791.
- 339 Lin, J. (2009). Divergence measures based on the Shannon entropy. *IEEE Transactions on Information Theory*,
340 37(1), 145–151.
- 341 Lohmann, G., Margulies, D. S., Horstmann, A., Pleger, B., Lepsien, J., Goldhahn, D., ... Turner, R. (2010).
342 Eigenvector centrality mapping for analyzing connectivity patterns in fMRI data of the human brain.
343 *PLoS One*, 5(4), e10232.
- 344 Lurie, D., Kessler, D., Bassett, D., Betzel, R., Breakspear, M., Keilholz, S., ... Calhoun, V. (2018). On the
345 nature of time-varying functional connectivity in resting fMRI. *PsyArXiv*, doi.org/10.31234/osf.io/xtzre.
- 346 Mairal, J., Ponce, J., Sapiro, G., Zisserman, A., & Bach, F. R. (2009). Supervised dictionary learning. *Advances*
347 *in Neural Information Processing Systems*, 1033–1040.

- 348 Mairal, J. B., Bach, F., Ponce, J., & Sapiro, G. (2009). Online dictionary learning for sparse coding. *Proceedings*
349 *of the 26th annual international conference on machine learning*, 689–696.
- 350 Manning, J. R., Ranganath, R., Norman, K. A., & Blei, D. M. (2014). Topographic factor analysis: a Bayesian
351 model for inferring brain networks from neural data. *PLoS One*, 9(5), e94914.
- 352 Manning, J. R., Zhu, X., Willke, T. L., Ranganath, R., Stachenfeld, K., Hasson, U., . . . Norman, K. A. (2018).
353 A probabilistic approach to discovering dynamic full-brain functional connectivity patterns. *NeuroImage*,
354 180, 243–252.
- 355 McInnes, L., & Healy, J. (2018). UMAP: Uniform manifold approximation and projection for dimension
356 reduction. *arXiv*, 1802(03426).
- 357 Newman, M. E. J. (2005). A measure of betweenness centrality based on random walks. *Social Networks*, 27,
358 39–54.
- 359 Newman, M. E. J. (2008). The mathematics of networks. *The New Palgrave Encyclopedia of Economics*, 2, 1–12.
- 360 Nocedal, J., & Wright, S. J. (2006). *Numerical optimization*. New York: Springer.
- 361 Opsahl, T., Agneessens, F., & Skvoretz, J. (2010). Node centrality in weighted networks: generalizing degree
362 and shortest paths. *Social Networks*, 32, 245–251.
- 363 Pearson, K. (1901). On lines and planes of closest fit to systems of points in space. *The London, Edinburgh,*
364 *and Dublin Philosophical Magazine and Journal of Science*, 2, 559–572.
- 365 Rao, C. R. (1982). Diversity and dissimilarity coefficients: a unified approach. *Theoretical Population Biology*,
366 21(1), 24–43.
- 367 Ricotta, C., & Szeidl, L. (2006). Towards a unifying approach to diversity measures: Bridging the gap
368 between the Shannon entropy and Rao's quadratic index. *Theoretical Population Biology*, 70(3), 237–243.
- 369 Rubinov, M., & Sporns, O. (2010). Complex network measures of brain connectivity: uses and interpreta-
370 tions. *NeuroImage*, 52, 1059–1069.
- 371 Schreiber, T. (2000). Measuring information transfer. *Physical Review Letters*, 85(2), 461–464.
- 372 Simony, E., Honey, C. J., Chen, J., & Hasson, U. (2016). Uncovering stimulus-locked network dynamics
373 during narrative comprehension. *Nature Communications*, 7(12141), 1–13.
- 374 Spearman, C. (1904). General intelligence, objectively determined and measured. *American Journal of*
375 *Psychology*, 15, 201–292.

- 376 Tipping, M. E., & Bishop, C. M. (1999). Probabilistic principal component analysis. *Journal of Royal Statistical*
377 *Society, Series B*, 61(3), 611–622.
- 378 Turk-Browne, N. B. (2013). Functional interactions as big data in the human brain. *Science*, 342, 580–584.
- 379 van der Maaten, L. J. P., & Hinton, G. E. (2008). Visualizing high-dimensional data using t-SNE. *Journal of*
380 *Machine Learning Research*, 9, 2579-2605.
- 381 Zar, J. H. (2010). *Biostatistical analysis*. Prentice-Hall/Pearson.